

## Local details versus effective medium approximation: A study of diffusion in microfluidic random networks made from Voronoi tessellations

Washington Ponce<sup>1</sup> and María Luisa Cordero<sup>2,\*</sup>

<sup>1</sup>*Departamento de Ciencias Exactas, Universidad de las Fuerzas Armadas ESPE - Extensión Santo Domingo, Vía Santo Domingo - Quevedo km. 24, Santo Domingo, Ecuador*

<sup>2</sup>*Departamento de Física, Facultad de Ciencias Físicas y Matemáticas, Universidad de Chile, Av. Blanco Encalada 2008, Santiago, Chile*



(Received 9 August 2019; revised manuscript received 6 January 2020; accepted 11 February 2020; published 26 February 2020)

We measured the effective diffusion coefficient in regions of microfluidic networks of controlled geometry using the fluorescence recovery after photobleaching (FRAP) technique. The geometry of the networks was based on Voronoi tessellations, and had varying characteristic length scale and porosity. For a fixed network, FRAP experiments were performed in regions of increasing size. Our results indicate that the boundary of the bleached region, and in particular the cumulative area of the channels that connect the bleached region to the rest of the network, are important in the measured value of the effective diffusion coefficient. We found that the statistical geometrical variations between different regions of the network decrease with the size of the bleached region as a power law, meaning that the statistical error of effective medium approximations decrease with the size of the studied medium with no characteristic length scale.

DOI: [10.1103/PhysRevE.101.023110](https://doi.org/10.1103/PhysRevE.101.023110)

### I. INTRODUCTION

Diffusion in porous media has been studied in several biological contexts, such as protein transport inside the cell [1,2], signaling in the brain [3,4], drug delivery in tumors [5], and transport of ions in muscles [6,7]. It is acknowledged that diffusion is slowed down in porous media both due to impenetrable obstacles that reduce the available space for diffusion and to the intricate trajectories that particles need to describe in order to circumvent the obstacles. The first effect can be quantified in terms of the porosity of the medium,  $\phi$ . The second effect is usually described in terms of tortuosity,  $\lambda > 1$ , which quantifies the increase in path length that diffusive particles travel within the medium. Hence, when diffusion of some species is measured in the porous medium filled with a given fluid, an average, or effective diffusion coefficient,  $D_{\text{eff}}$ , is obtained, which is smaller than the diffusion coefficient that would be measured for the same species in the same fluid but in free space,  $D_0$ .

Typical experimental values of  $D_{\text{eff}}/D_0$  are  $\approx 0.44$  for packed beds of beads [8],  $\approx 1$  for the brain extracellular space [4], and between 0.23 and 0.59 for the endoplasmic reticulum [9]. In real biological situations, however, one has to deal with complex processes that further slow down the diffusive transport, such as a usually unknown viscosity of the ambient fluid, binding of the diffusive molecules to macromolecular complexes, hindering to diffusion due to molecular crowding [10,11] or geometrical blockage of large diffusive molecules in narrow passages [12], and permeating boundaries [13]. In order to assess the relevance of these effects, it would be desirable to isolate them from the purely geometrical ones of the medium.

Theoretical models describing the porous medium as the space around a loosely packed bed of solid spheres [14], or a collection of twisted capillaries [15], yield values of  $D_{\text{eff}}/D_0$  of the same order of magnitude as experiments. However, these models have poor predictive power when applied to real cases, since it is not clear if they capture the essential geometrical features of a particular medium. Numerical simulations have delivered useful information [16], but due to practical limitations they have usually simplified the studies to periodic lattices of polyhedral obstacles [17], which are inherently anisotropic and unrealistic.

Effective medium approximations have been developed to describe the effective diffusion coefficient of porous media based on Voronoi and Delaunay tessellations [18–20]. Effective medium approximations imply a description over a length scale much larger than any characteristic geometrical length scale of the medium. In this way, local geometrical details are averaged and only global features emerge. However, measurements and simulations of diffusion in porous media are performed in samples of finite size or in reduced regions within a sample, and hence the results can reflect the effective properties of the medium and/or local details of the measurement position [21]. The correct description of a porous medium as an effective one depends on the correct determination of a minimum length scale over which the medium can be described as an effective one. We explore this idea by studying diffusion in networks of channels at different length scales compared to the characteristic scale of the networks. For this, we propose an experimental approach in which two-dimensional networks of microchannels are fabricated from Voronoi tessellations to simulate random, globally isotropic porous media. We measure the diffusion of fluorescein in water, a small molecule for which geometrical hindering is negligible in the micrometric channels used,

\*[mcordero@ing.uchile.cl](mailto:mcordero@ing.uchile.cl)

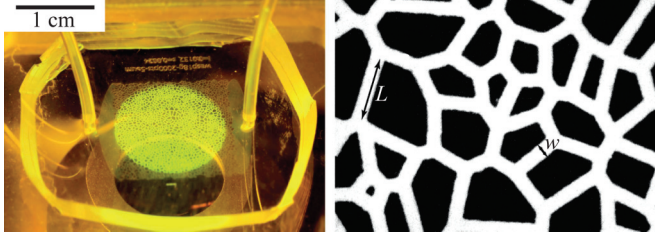


FIG. 1. Left: Photography of an assembled microfluidic channel. Inlet and outlet tubes are visible. Right: Fluorescence micrograph of a region of one microfluidic network. White areas correspond to channels, filled with the fluorescent solution.

as well as binding and permeation through the walls. The diffusive properties of the networks are measured locally in different regions of the sample with the fluorescence recovery after photobleaching (FRAP) technique [22–25]. In order to test the accuracy of the effective medium approximation, the dispersion of the measured diffusivity in different places of the networks is monitored as the size of the measurement regions is systematically increased. Our results are then qualitatively explained with a simple model that relates the effective diffusivity measured with the FRAP technique to the permeable perimeter of the measurement region.

II. MATERIALS AND METHODS

A. Design of networks

Random networks of channels were designed and fabricated [26]. Briefly, Voronoi polygons were generated from a set of  $n$  random seed points inside a square region of sides 15 mm. The edges of the Voronoi polygons, which become the microchannels after the fabrication process, were then assigned with a given width  $w$  between 13  $\mu\text{m}$  and 125  $\mu\text{m}$ . The disorder of the network can be adjusted from the initial set of seed points, by imposing a minimum distance  $d$  between any pair of points. This is quantified by the parameter  $\alpha = d/d_0$ , where  $d_0 = \sqrt{2A_0/(n\sqrt{3})}$  is the distance between the seed points in a completely regular network (a honeycomb network),  $A_0 = (15 \text{ mm})^2$  being the area of the square region [27]. Hence,  $\alpha = 1$  corresponds to a completely regular honeycomb lattice, while disorder increases as  $\alpha$  decreases. In our study, we arbitrarily fixed  $\alpha = 0.3$ .

Inlet and outlet sections were added at opposite sides of the network, and then the designs were used to fabricate negative masters of the microchannels through optical lithography in SU-8 photoresist (GM1070, Gersteltech Sarl). The height of the molds was set at 50  $\mu\text{m}$ . From the masters, microfluidic networks were fabricated in polydimethylsiloxane (PDMS) (Sylgard 184, Dow Corning) using standard soft lithography techniques [28]. Inlet and outlet access holes were punched before sealing the PDMS networks against a glass slide by oxygen plasma activation. An example of a microfluidic network is shown in Fig. 1.

For each network we can control the number  $n$  of seed points, which determines an average length channel  $\langle L \rangle$ . Independently, we can control the width  $w$  of the channels. Larger channel width increases the porosity  $\phi$  of the network, which

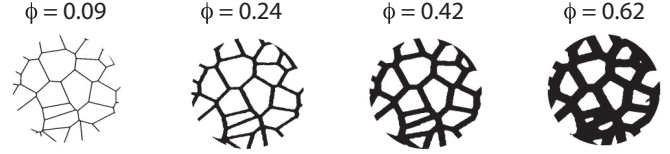


FIG. 2. Micrographies of networks with different porosities (networks B–E from Table I). As the width of the channels increases, the reticular aspect of the network is lost. Color is inverted, so dark regions represent fluorescent-filled channels.

we define as usual,

$$\phi = \frac{A_{\text{channel}}}{A_0}, \tag{1}$$

where  $A_{\text{channel}}$  is the total area of the microchannels in the network. As  $\phi$  increases, the network resembles less a collection of narrow channels, as shown in Fig. 2.

Several designs with different number of seed points and different channel widths, hence different  $\phi$ , were fabricated. All the channels used in this study are listed in Table I.

Besides the random networks, one circular chamber of diameter 1.5 cm and height 50  $\mu\text{m}$  was fabricated with SU-8 walls on a glass slide, filled with the fluorescent solution and closed with a cover slip in order to measure diffusion in free, two-dimensional space. Finally, a flow-focusing microchannel was used to measure the diffusion coefficient in flow by measuring the widening of a central fluorescent solution sheathed by two water streams [29].

B. FRAP experiments

After fabrication, the networks were filled with an aqueous solution of fluorescein (Kingscote Chemicals) at a concentration of 0.5 mM. Microchannels were mounted on an inverted microscope (Nikon TS100) with epifluorescence illumination, and observed with a CMOS camera (DCC1545M, Thorlabs) at a rate between 1 and 1/5 frames per second (fps).

The effective diffusion coefficient of fluorescein was measured through the FRAP technique. The technique consists in irreversibly inactivating (bleaching) the fluorescence of fluorescein molecules with a high intensity excitation illumination in a small region. Afterwards, fluorescence is observed with a lower intensity excitation illumination. As bleached molecules diffuse out of, and nonbleached fluorescent molecules diffuse into the bleached area, the fluorescence is recovered in the bleached region. Fluorescence recovery curves are then fitted with a model based on the diffusion equation [30,31] (see the Appendix for details on the fitting

TABLE I. Networks used within this study.

| Network | $n$   | $\langle L \rangle (\mu\text{m})$ | $w (\mu\text{m})$ | $\phi$ |
|---------|-------|-----------------------------------|-------------------|--------|
| A       | 500   | 458                               | 82                | 0.22   |
| B       | 2000  | 227                               | 13                | 0.09   |
| C       |       |                                   | 38                | 0.24   |
| D       |       |                                   | 75                | 0.42   |
| E       |       |                                   | 125               | 0.62   |
| F       | 10000 | 101                               | 24                | 0.25   |

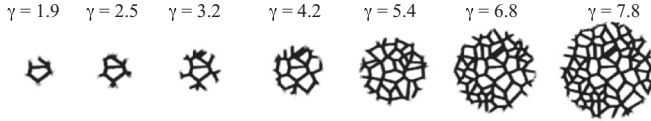


FIG. 3. Color-inverted micrographies of bleached areas with different  $\gamma$ . Images correspond to network E in Table I.

procedure) and an effective diffusion coefficient is obtained. In our experiments, bleaching was achieved using the highest intensity of the epifluorescence excitation illumination, focused into the sample with a 10X, 0.25 NA objective during 5 s. The radius  $R$  of the bleached area was controlled with a diaphragm between  $134 \mu\text{m}$  and  $1.4 \text{ mm}$ . The time scale for diffusion in a two-dimensional circle of radius  $R$  is given by

$$\tau_0 = \frac{R^2}{4D_0}. \quad (2)$$

Considering the diffusion coefficient of fluorescein in water at room temperature, which was measured at  $D_0 = 6.66 \times 10^{-10} \text{ m}^2/\text{s}$  (see Sec. III A),  $\tau_0$  ranges between  $\tau_0 = 7 \text{ s}$  and  $\tau_0 = 454 \text{ s}$  for the given values of  $R$ . For the smaller values of  $R$ , the bleaching duration is not negligible in front of  $\tau_0$ . However, our fitting method uses an approximate initial condition after the bleaching, as explained in the Appendix.

Recovery of the fluorescence was observed through a 2X, 0.06 NA objective using a dimmed excitation illumination to minimize further bleaching (1/32 times the intensity used for bleaching), during a period of time that ranged between 15 min and 60 min, depending on  $R$ .

Depending on the radius of the bleached zone, more or less details of the network are included in the bleached area. To quantify the effect of geometrical details on the recovery of fluorescence, we define the homogeneity parameter

$$\gamma = \frac{R}{\langle L \rangle}. \quad (3)$$

A value of  $\gamma < 1$  indicates that only a fraction of a straight channel is bleached. On the other hand,  $\gamma \gg 1$  means that many straight segments of the networks are included in the bleached area, and geometric details of the network are averaged in the bleached region. Examples of different bleached areas with various values of  $\gamma$  are shown in Fig. 3.

### C. Recovery curves

Recovery curves were obtained in the following manner. Prior to the experiment, a prebleaching image of the network was recorded with the 2X objective and low excitation intensity. A binary mask  $M$  of the bleached region was obtained by dividing the prebleached image and the first postbleaching image, then binarizing with application of a threshold [see Figs. 4(a)–(c)]. A complementary mask,  $M^c$  was also obtained by subtracting the mask  $M$  to the binarized prebleaching image, as shown in Fig. 4(d). The average fluorescence in the bleached and complementary regions were then computed as

$$F_{\text{in}} = \frac{\sum_{i,j} I_{ij}(t)M_{ij}}{\sum_{i,j} M_{ij}}, \quad (4)$$

$$F_{\text{out}} = \frac{\sum_{i,j} I_{ij}(t)M_{ij}^c}{\sum_{i,j} M_{ij}^c}, \quad (5)$$

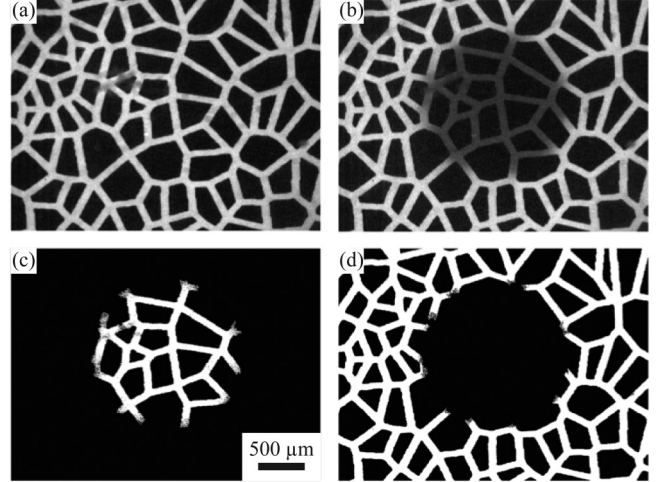


FIG. 4. Procedure for obtaining the bleached and complementary masks. (a) Image before photobleaching. (b) First image after photobleaching. (c) and (d) Bleached and complementary masks.

where  $I_{ij}(t)$  represents the gray value of the pixel  $(i, j)$  of the postbleaching image  $I$  at time  $t$ , and  $M_{ij}$  and  $M_{ij}^c$  represent the value of the masks  $M$  and  $M^c$  at the pixel  $(i, j)$ .

As fluorescent molecules diffuse into, and bleached molecules diffuse out of the bleached area, the average fluorescence of the bleached area,  $F_{\text{in}}$  increases and the average fluorescence of the complementary region,  $F_{\text{out}}$ , decreases. However, unwanted, inhomogeneous, non-negligible bleaching occurs during observation of the fluorescence recovery, causing  $F_{\text{in}}(t)$  not to increase monotonically, and  $F_{\text{out}}(t)$  to decrease both due to diffusion and bleaching, as shown in Fig. 5(a). To correct for this, images of the same region of the microfluidic network are obtained with the same illumination and acquisition protocol, but without the initial bleaching. In this way, only the bleaching due to observation is recorded as a reference. The average fluorescence of the bleached and complementary regions for these reference images are computed in the same way, as

$$F_{\text{in}}^{\text{ref}} = \frac{\sum_{i,j} I_{ij}^{\text{ref}}(t)M_{ij}}{\sum_{i,j} M_{ij}}, \quad (6)$$

$$F_{\text{out}}^{\text{ref}} = \frac{\sum_{i,j} I_{ij}^{\text{ref}}(t)M_{ij}^c}{\sum_{i,j} M_{ij}^c}, \quad (7)$$

where  $I_{ij}^{\text{ref}}$  represents the gray value of pixel  $(i, j)$  of the reference image  $I^{\text{ref}}$  at time  $t$ . Hence, the fraction of fluorescence recovered due to diffusion in the bleached area with respect to the complementary region is defined as

$$F(t) = \frac{F_{\text{in}}(t)/F_{\text{in}}^{\text{ref}}(t)}{F_{\text{out}}(t)/F_{\text{out}}^{\text{ref}}(t)}. \quad (8)$$

Effective diffusion coefficients are obtained by adjusting  $F(t)$  to a numerically obtained model recovery curve, similar to what is described in Ref. [30] but taking into account the intensity profiles for observation and bleaching, as explained in the Appendix. The recovery curve  $F(t)$  is not normalized between 0 and 1, as is usually done, in order to increase the sensitivity of the fit. An example of a recovery curve  $F(t)$  together with the best fit is shown in Fig. 5(b).

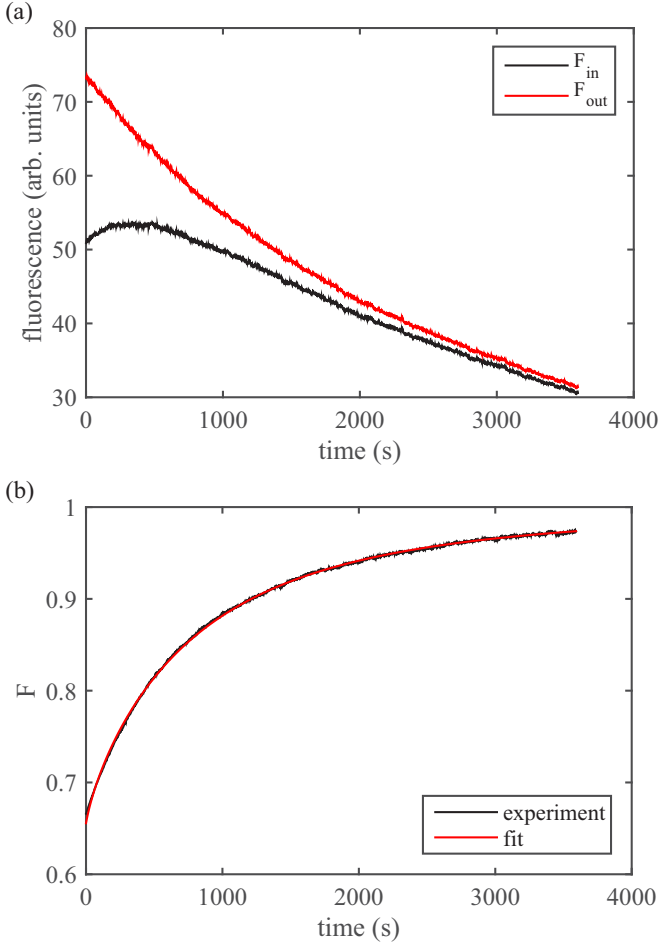


FIG. 5. (a) Evolution of the average fluorescence of the bleached and complementary regions. (b) Recovery curve  $F(t)$  and the corresponding fit. The curves corresponds to a FRAP experiment in network F with  $\gamma = 13.2$ .

The fitting procedure has two fitting parameters, the amount of bleaching,  $G$ , and the characteristic time scale

$$\tau = \frac{R^2}{4D_{eff}}, \quad (9)$$

from which the effective diffusion coefficient,  $D_{eff}$ , is obtained.

### III. RESULTS

#### A. Absolute diffusion coefficient of fluorescein

The absolute diffusion coefficient of fluorescein in water,  $D_0$ , was measured in two different ways. First, FRAP measurements were performed in the circular quasi-two-dimensional chamber. Two different bleaching radii were used,  $R_1 = 198 \mu\text{m}$  and  $R_2 = 567 \mu\text{m}$ . The same numerical fitting procedure used in the random networks was employed here, yielding the values of  $D_0^{(1)} = (6.77 \pm 0.23) \times 10^{-10} \text{ m}^2/\text{s}$  and  $D_0^{(2)} = (6.35 \pm 0.25) \times 10^{-10} \text{ m}^2/\text{s}$ , respectively. Errors represent the standard deviation of five repetitions, and are below 5%.

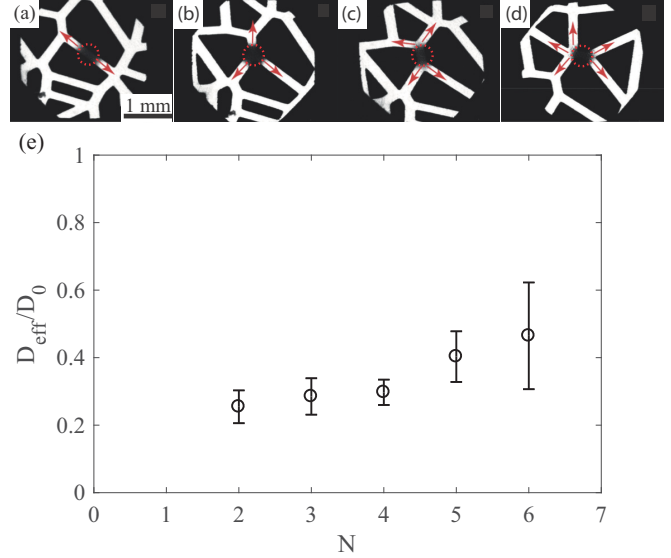


FIG. 6. (a)–(d) Images of FRAP experiments with varying number of feeding channels. All cases correspond to network A in Table I. Dashed red circles indicate the bleached region. (e) Normalized effective diffusion coefficient,  $D_{eff}/D_0$  for different number of feeding channels,  $N$ .

In order to validate our fitting model, the diffusion coefficient was determined independently in the flow-focusing microchannel as reported in Ref. [29] and compared to the values presented above. Briefly, a central stream of the fluorescent solution and two flanking water streams were injected at constant flow rates. For a fixed location of the microchannel, the fluorescence intensity profile of the central stream was obtained and fitted to a Gaussian curve. The width of the Gaussian curve increases with the downstream location, from which the diffusion coefficient was obtained at  $D_0^{(3)} = (6.87 \pm 0.61) \times 10^{-10} \text{ m}^2/\text{s}$ . The error corresponds to the standard deviation of seven measurements performed with different flow rates.

All results thus obtained agree within experimental error, which validates our fitting procedure. In average, the free-space diffusion coefficient for fluorescein in water was considered to be  $D_0 = (6.66 \pm 0.69) \times 10^{-10} \text{ m}^2/\text{s}$ .

#### B. Number of feeding channels

We investigate the effective diffusion coefficient in small bleached regions located at the intersection between channels, as shown in Figs. 6(a)–6(d). The objective is to establish the role that the number of channels that converge into the bleached region,  $N$ , has in the recovery process. These experiments were performed in network A with a bleaching radius  $R = 251 \mu\text{m}$ , which is smaller than the average length of the network’s channels ( $\gamma = 0.5$ ).

For each number  $N$  of converging channels, five regions were randomly selected in the network. The average effective diffusion coefficient,  $D_{eff}$ , normalized by  $D_0$  is plotted as a function of the number of feeding channels in Fig. 6(e), with error bars representing the standard deviation of the five measurements. The effective diffusion coefficient increases

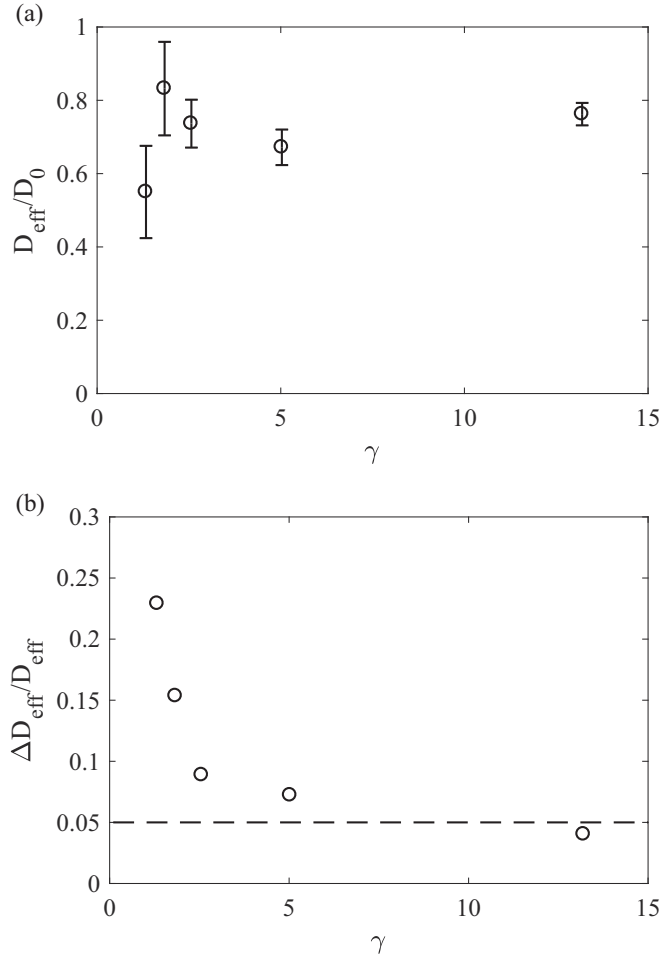


FIG. 7. (a) Normalized effective diffusion coefficient,  $D_{\text{eff}}/D_0$  as a function of  $\gamma$  for network F. (b) Standard deviation of  $D_{\text{eff}}$ , normalized by  $D_{\text{eff}}$ , for ten realizations in arbitrary locations of the same network, at fixed  $\gamma$ . The dashed line marks the 5% accuracy limit of our measurements.

with the number of feeding channels, from a value of  $\approx 0.25D_0$  for  $N = 2$  to  $\approx 0.45D_0$  when  $N = 6$ .

**C. Effective medium**

In order to determine the minimum radius  $R$  for which the network can be considered as an effective medium, we performed FRAP experiments using a single network (network F from Table I) and we vary the size of the bleached region, from  $\gamma = 1.33$  ( $R = 134 \mu\text{m}$ ) to  $\gamma = 13.59$  ( $R = 1373 \mu\text{m}$ ). For each value of  $\gamma$ , ten FRAP experiments were performed in random locations of the network to obtain an effective diffusion coefficient  $D_{\text{eff}}$  and its statistical variation  $\Delta D_{\text{eff}}$  from the average and standard deviation of the obtained coefficients.

The results are shown in Fig. 7. In all cases,  $D_{\text{eff}}/D_0 < 1$ , indicating that the geometry of the network slows down the diffusion coefficient, as expected. The average values of  $D_{\text{eff}}$  vary between  $0.55D_0$  and  $0.62D_0$  in a nonmonotonic way as  $\gamma$  is increased in a decade [Fig. 7(a)].

The dependence of the fractional error  $\Delta D_{\text{eff}}/D_{\text{eff}}$  with  $\gamma$  is shown in Fig. 7(b). For a small bleached area, the dispersion in the fitted diffusion coefficient is larger than 20%. As the

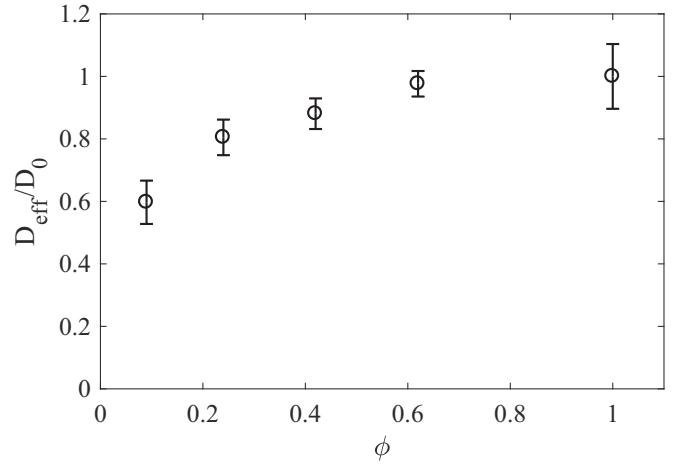


FIG. 8. Normalized effective diffusion coefficient,  $D_{\text{eff}}/D_0$  as a function of the porosity  $\phi$  for fixed  $\gamma = 3.99$ .

size of the bleached region increases,  $\Delta D_{\text{eff}}$  rapidly decreases. For  $\gamma \gtrsim 10$ ,  $\Delta D_{\text{eff}}$  becomes comparable to the characteristic error of the method, which is estimated at  $\approx 5\%$  [dashed line in Fig. 7(b)], according to the measurements for  $D_0$  presented in Sec. III A.

**D. Available area**

Finally, in order to determine the effect of the available area for diffusion, we perform experiments in networks with the same geometry but varying channel width (networks B–E from Table I). In these networks, the original Voronoi polygons are the same, and only the channel width is varied. In all cases, we fix the size of the bleached region at  $\gamma = 3.99$  ( $R = 790 \mu\text{m}$ ). Six locations were randomly chosen in the geometry to perform the FRAP experiments. We used the same six bleaching positions in all networks, as can be noted in Fig. 2, although minor displacements occurred between different networks.

The results are shown in Fig. 8. The point  $\phi = 1$  corresponds to a hypothetical network for which channels are so wide that merge into a quasi-two-dimensional chamber, in which case the absolute diffusion coefficient  $D_0$  should be recovered. The error bar in this case corresponds to the propagated error of the three different measured values of  $D_0$  (Sec. III A). As channels become more slender and  $\phi$  decreases, the normalized effective diffusion coefficient decreases. In these cases, the error bars represent the standard deviation in the  $D_{\text{eff}}$  obtained in all six locations for each network. Note that, for the chosen size of the bleached region, the dispersion in the results between different regions is expected to be higher than the precision of the method (5%), which is consistent with the values obtained for the error bars (between 5% and 11%).

**IV. MODEL FOR DETERMINATION OF A CHARACTERISTIC LENGTH SCALE**

FRAP experiments in small regions of our random networks of channels, presented in Sec. III B, demonstrate the relevance of the number of channels that feed the bleached region with the diffusing species. On the other hand, the

dependence of  $D_{\text{eff}}$  with the size of the bleached region was studied in Sec. III C, in an attempt to establish the scale at which the random network can be approximated as an effective medium. In order to relate these two results, we present here a model based on the diffusion equation and on the statistical characteristics of the geometries used to fabricate the networks.

Consider, similarly to the experiments, the region consisting of the intersection between a two-dimensional random network and a circle of radius  $R$ , to which we call  $\Omega$ . Assuming an excitation illumination of uniform intensity,  $I$ , the fluorescence recorded within  $\Omega$  is given by

$$F_{\Omega}(t) = qI \int_{\Omega} c(r, t) d^2r, \quad (10)$$

where  $c(r, t)$  is the concentration of nonbleached fluorescein molecules and  $q$  is a constant that accounts for all efficiencies of absorption, emission and detection of fluorescence. In the following, we will omit the constants  $q$  and  $I$ .

Neglecting the unwanted bleaching due to observation that occurs in the experiments, the rate of change of fluorescence recorded within the region is given by the incoming flux of fluorescent molecules into  $\Omega$ . In comparison with free space, where the diffusive flux comes across the whole circumference of radius  $R$ , in the random network the incoming flux comes only through the  $N$  feeding channels that intersect the circumference,

$$\dot{F}_{\Omega}(t) = - \sum_{i=1}^N J_i. \quad (11)$$

The fluxes  $J_i$  are given by Fick's first law integrated in the corresponding portion of the circumference, of perimeter  $\mathcal{P}_i$ , and oriented at an angle  $\theta_i$ ,

$$J_i = -D_0 \int_{\mathcal{P}_i} \nabla c \cdot \hat{r} d\ell \approx -D_0 \left. \frac{\partial c}{\partial r} \right|_{(R, \theta_i, t)} \mathcal{P}_i. \quad (12)$$

Assuming isotropy, we write

$$\dot{F}_{\Omega}(t) = D_0 \left. \frac{\partial c}{\partial r} \right|_{(R, t)} \sum_{i=1}^N \mathcal{P}_i \quad (13)$$

$$= D_{\text{eff}} 2\pi R \left. \frac{\partial c}{\partial r} \right|_{(R, t)}, \quad (14)$$

where we can identify the effective diffusion coefficient as

$$D_{\text{eff}} = \frac{D_0}{2\pi R} \sum_{i=1}^N \mathcal{P}_i. \quad (15)$$

This suggests that an important feature of a patterned space in its diffusing properties, at least as measured with FRAP experiments, is the fraction of open area that transports the diffusing species into the bleached region. This picture is incomplete, since the concentration field in the effective medium, say  $c_{\text{eff}}$ , is different to the actual concentration of the species,  $c$ , and should appear in Eq. (14). However, if we assume that the argument is qualitatively correct, it yields to an interesting conclusion regarding the definition of a length scale appropriate to define an effective medium, at least in channels based of Voronoi polygons like ours, as we shall present next.

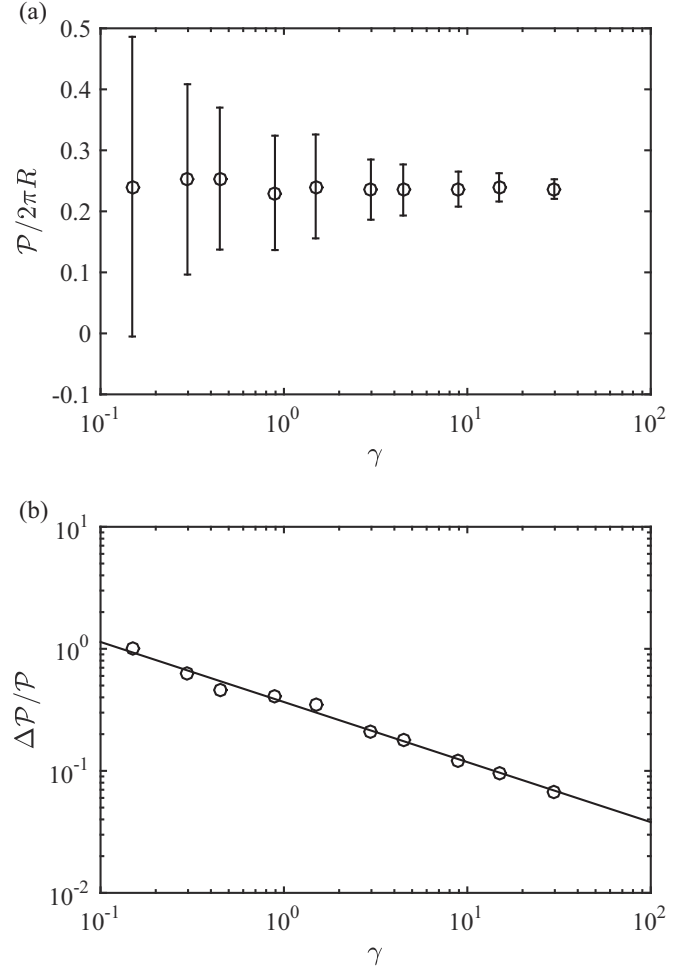


FIG. 9. (a) Perimeter fraction of feeding channels as a function of  $\gamma$ . (b) Fractional error of the perimeter fraction of feeding channels as a function of  $\gamma$ . The solid line represents the fit of Eq. (16).

As illustration, we consider the geometry of network F in Table I. All initial Voronoi polygons were stored in a MATLAB routine and shrunk to produce the simulated network of 24  $\mu\text{m}$ -wide channels. At 121 equally spaced locations, circles of increasing radius  $R$  were drawn and the total perimeter of feeding channels,  $\mathcal{P} = \sum \mathcal{P}_i$ , was computed for each location and radius. Results are presented in Fig. 9 as a function of  $\gamma$ , which is defined, as in the experiments, as  $\gamma = R/\langle L \rangle$ . The average perimeter fraction,  $\mathcal{P}/2\pi R$ , is shown in Fig. 9(a). Little variation occurs in the whole investigated range of  $\gamma$ , which spans over two decades. Error bars represent the standard deviation of the perimeter fraction,  $\Delta\mathcal{P}/2\pi R$ , which decrease dramatically as  $\gamma$  increases. Figure 9(b) presents the normalized standard deviation of  $\mathcal{P}$ . As demonstrated by the linear trend in the log-log plot,  $\Delta\mathcal{P}/\mathcal{P}$  follows a power law with  $\gamma$ , which was fitted as

$$\frac{\Delta\mathcal{P}}{\mathcal{P}} = 0.34 \gamma^{-0.49}. \quad (16)$$

The fractional error,  $\Delta\mathcal{P}/\mathcal{P}$ , is important to determine whether or not the network can be considered as an effective medium at the scale  $\gamma$ . Here,  $\Delta\mathcal{P}/\mathcal{P}$  quantifies the effects of geometrical variation of inlet area between the different

regions of the random network, and thus, for a truly effective medium in which the location of measurement is irrelevant,  $\Delta\mathcal{P}/\mathcal{P}$  should be zero. Our results indicate that  $\Delta\mathcal{P}/\mathcal{P}$  decreases with  $\gamma$ , i.e., that the variations in geometry between different regions decrease as the size of the considered region increases. Although the power law does not allow us to determine a characteristic length scale over which the effective medium approximation can be used, our results do indicate that the statistical differences between regions can be made as small as wanted by considering sufficiently large regions. Typically, one should aim to decrease the dispersion to the accuracy limit of the method, which was estimated at 5% in our case. Experimentally, for our Voronoi-based random networks, this limit was reached for bleached regions of radius approximately 10 times larger than the mean cell length [Fig. 7(b)].

## V. DISCUSSION

We have presented here an experimental approach to investigate the relevance of the geometry of porous media to diffusion properties measured with the FRAP technique. Our experiments are performed in controlled microfluidic environments, whose geometry is based on Voronoi polygons. However, other two-dimensional geometries can be used as well, such as assemblies of circular obstacles or regular polygons. This could be interesting in order to determine the relevance of geometrical features that are not present in the Voronoi tessellations, such as dead ends, large accumulation chambers, or large-scale anisotropy. Moreover, a similar microfluidic approach could complement recent efforts in the numerical reconstruction of cellular structures [9,32]. Indeed, microfluidic networks of virtually any two-dimensional geometry can be fabricated, which can aid in determining the role of geometry in the diffusive transport. Unfortunately, however, no standardized methods exist yet to fabricate complex three-dimensional microfluidic geometries, limiting the applicability of this idea to two-dimensional networks.

The method used in this work to generate the porous media, based on Voronoi polygons, can be used to vary independently the whole geometry of the network (i.e., its tortuosity) by changing the seed points used to generate the polygons, or its porosity, by changing the width of the channels. Keeping constant the tortuosity of the networks demonstrates the relevance of the porosity in the effective diffusion coefficient (networks B–E and Fig. 8). It is less evident to keep the porosity constant and vary the tortuosity in a systematic way. Comparison between networks C [ $\phi = 0.24$ ,  $D_{\text{eff}} = (0.80 \pm 0.06)D_0$ , see Fig. 8] and F [ $\phi = 0.25$ ,  $D_{\text{eff}} = (0.76 \pm 0.03)D_0$ , Fig. 7(a)] suggests that reduction of available space, and not the particular path length, is the major geometric source of the slowing down of diffusion in porous media compared with free space. These results are consistent with existing work with aligned and staggered polygons [5].

The FRAP technique that we have used measures long-time, large-scale, collective diffusion of fluorescent molecules. Unlike other methods based on single molecule tracking, FRAP is unable to detect anomalous diffusive behavior. Hence, no length scale can be extracted below which subdiffusive behavior occurs [21,33]. Although at larger scales

simple diffusive transport is recovered, the obtained values of  $D_{\text{eff}}$  only correspond to the effective property of the network if the bleached region is sufficiently large to contain enough geometrical information of the network. Our experiments with increasing size of the bleached region show that, in general, the measured  $D_{\text{eff}}$  decrease for larger bleached areas [Fig. 7(a)], which is consistent with previous works [33]. For  $\gamma \gtrsim 3$ , variation in  $D_{\text{eff}}$  is less important, suggesting that we have reached the simple diffusion regime.

For small regions where the number  $N$  of feeding channels can be easily counted,  $D_{\text{eff}}$  was found to increase with  $N$ . At this small scale neither the effective medium approximation nor the simple diffusion regime are expected to hold. Hence, the values of  $D_{\text{eff}}$  found in these experiments do not represent the effective diffusivity of the network, but reflect local details in and around the bleached region. Therefore, these results indicate only that fluorescence recovers faster when the number of feeding channels is larger.

For larger regions, where  $N$  is not easily determined, we have measured values of  $D_{\text{eff}}$  that fluctuate around a mean value, with a dispersion that decreases as the size of the bleached region increases. To explain both results, we have presented a simple model, which states that the dispersion of the effective diffusion coefficient measured in different regions can be explained by the variations of the perimeter fraction that connects the bleached and the outer regions. From the model, we found no characteristic length scale over which these variations become negligible. Note that this does not mean that no characteristic length scale could be defined for a Voronoi network in other ways. Indeed, a characteristic length scale can be defined, for example, as the mean length of the Voronoi polygons edges, which corresponds to  $L$  in our case. However, we have failed in relating this length scale to an appropriate size for which the network can be statistically approximated to a homogeneous medium. Also, our finding does not prevent the existence of a mean effective diffusion coefficient for each Voronoi network, and hence a corresponding effective medium description. Instead, we find that the value of  $D_{\text{eff}}$  measured at different locations of the network will present deviations around the mean value, and that these statistical variations decrease as a power law with the size of the bleached region, with exponent  $\approx -0.5$ , and thus can be made as small as the inherent accuracy limit of the FRAP method.

## VI. CONCLUSIONS

In conclusion, we have presented an experimental approach to measure the effective diffusion coefficient of networks of channels, isolating the geometrical effects only. Our networks are random collections of channels based on Voronoi tessellations. Systematic FRAP measurements with increasing sizes of the bleached region show that the effective medium approximation improves as the bleached region increases. We have shown that the measured effective diffusivities fluctuate around a mean value with a dispersion that decreases as the measurement region increases. Our model suggests that this dispersion decreases as a power law with the size of the bleached region.

These results call for caution in the analysis of FRAP experiments in biological systems, where bleaching a sufficiently large region is not necessarily possible and multiple equivalent regions in the same system may not be available. Several measurements in different samples is a logical choice, and in that case, together with the natural geometrical variability that can occur between samples, one should consider also the error associated to the finite extent of the bleached region in the effective medium approximation.

### ACKNOWLEDGMENTS

Useful discussions with Jorge Toledo are gratefully appreciated. MLC acknowledges support of CONICYT, FONDECYT Grant No. 1170411 (Chile) and Millennium Nucleus Physics of Active Matter of ANID (Chile). Molds for the microfluidic networks were fabricated in the Laboratory of Optical Lithography, built thanks to CONICYT, FONDECYT Grants No. EQM140055 and No. EQM180009 (Chile). WP acknowledges funding from Secretaría de Educación Superior, Ciencia y Tecnología del Ecuador.

### APPENDIX: MODEL FITTING

The model used for fitting differs from traditional models [30] in the use of the measured profiles of the bleaching and observation illumination intensities, similar to Ref. [34]. For the model, we define the intensity in the bleached and outer regions,  $F_{\text{in}}^{\text{model}}$  and  $F_{\text{out}}^{\text{model}}$ , assuming that they are proportional to the concentration of nonbleached fluorescent molecules,  $c(r, t)$  and to the excitation intensity of the observation illumination,  $I_{\text{obs}}(r)$ ,

$$F_{\text{in}}^{\text{model}} = 2\pi \int_0^R I_{\text{obs}}(r) c(r, t) d^2r, \quad (\text{A1})$$

$$F_{\text{out}}^{\text{model}} = 2\pi \int_R^{R_{\text{out}}} I_{\text{obs}}(r) c(r, t) d^2r. \quad (\text{A2})$$

In Eq. (A2), we defined  $R_{\text{out}}$  as the radius of the largest circle that can be inscribed within the field of view.

The concentration is obtained from the solution of the diffusion equation using the Fourier transform,

$$c(r, t) = \frac{1}{2\pi} \int e^{-i\vec{k}\cdot\vec{r}} \hat{c}(k, 0) e^{-D_{\text{eff}}k^2t} d^2k, \quad (\text{A3})$$

where  $\hat{c}(k, 0)$  is the Fourier transform of the concentration profile at  $t = 0$ . Note that we are assuming radial symmetry and the existence of an effective medium.

Let  $I_b(r)$  be the bleaching illumination profile, then

$$c(r, 0) = c_0 e^{-G I_b(r)}, \quad (\text{A4})$$

where  $G$  is the product between the absorption coefficient of the fluorescent solution and the duration of the bleaching.

After some algebra we obtain

$$F_{\text{in}}^{\text{model}} = \int_0^\infty \frac{\alpha J_1(K\alpha)}{K} (K\phi(K) - J_1(K)) e^{-K^2T} dK + \frac{\alpha^2}{2}, \quad (\text{A5})$$

$$F_{\text{out}}^{\text{model}} = \int_0^\infty \frac{J_1(K) - \alpha J_1(K\alpha)}{K} (K\phi(K) - J_1(K)) e^{-K^2T} dK + \frac{1 - \alpha^2}{2}, \quad (\text{A6})$$

where  $\alpha = R/R_{\text{out}}$ ,  $K = kR$ ,  $T = t/\tau$ , and the auxiliary function  $\phi$  is

$$\phi(K) = \int_0^1 e^{-G I_b(r)} J_0(Kr) r dr. \quad (\text{A7})$$

The model equation used for fitting is, then

$$F^{\text{model}} = \frac{F_{\text{in}}^{\text{model}}}{F_{\text{out}}^{\text{model}}}. \quad (\text{A8})$$

In order to obtain the observation and bleaching illumination profiles, we used the circular quasi-two-dimensional chamber. For the observation illumination profile, we assumed that the concentration of nonbleached fluorescent molecules is uniform before any measurement. One prebleaching image,  $F_0$ , was obtained and averaged over circular regions of one pixel width. The resulting profile is, up to a constant, equal to the observation illumination profile  $I_{\text{obs}}$ . Since the constant cancels out in Eq. (A8), we normalize the result by the value at  $r = 0$ , where the observation illumination intensity is largest.

For the bleaching illumination profile, the solution was bleached for 5s with the corresponding diaphragm aperture and one image,  $F_b$ , was immediately obtained. This image was divided pixel by pixel by the reference one,  $F_0$ , and the result was averaged over circular regions of one pixel width. The result, according to Eq. (A4) corresponds to

$$\frac{F_b(r)}{F_0(r)} = e^{-G I_b(r)}. \quad (\text{A9})$$

To eliminate the factor  $G$ , we use the value at the center,

$$\frac{I_b(r)}{I_b(0)} = \frac{\ln [F_b(r)/F_0(r)]}{\ln [F_b(0)/F_0(0)]}. \quad (\text{A10})$$

The constant  $I_b(0)$  can be absorbed in  $G$ , so its value is irrelevant.

For small values of  $R$ , the characteristic diffusion time scale  $\tau_0$  may be comparable to the 5 s of bleaching time. In fact, the postbleaching image  $F_b$  corresponds to the initial condition for diffusion in the quasi-two-dimensional chamber, and includes the diffusive transport that occurs during the bleaching. Therefore, our measured  $I_b$  can be considered as

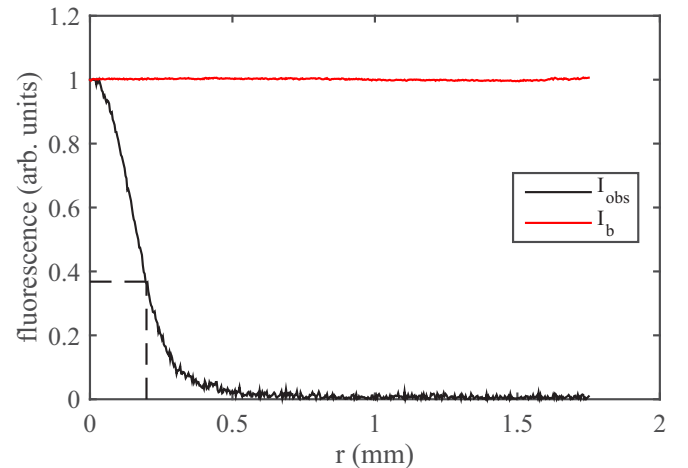


FIG. 10. Examples of observation and bleaching profiles. The dashed lines show  $R = 198 \mu\text{m}$  and  $1/e$ .

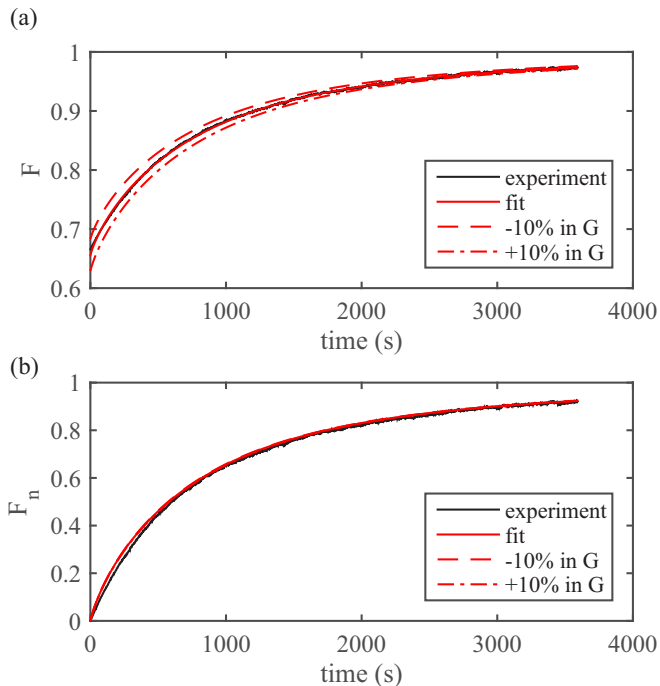


FIG. 11. (a) Recovery curve (black line) and best fit (red line). The dashed and dot-dashed lines represent the model curves with  $G$  decreased and increased in 10%, respectively. In (b), the same curves are normalized between 0 and 1. The curves with  $G$  decreased and increased in 10% are virtually indistinguishable from the best fit.

the bleaching profile that would lead to the measured initial condition if the bleaching was instantaneous.

Figure 10 shows the observation and bleaching illumination profiles obtained for  $R = 198 \mu\text{m}$ . The bleaching radius  $R$  was obtained from the bleaching profile as the location where  $I_b$  falls below  $1/e$ . Note that the observation profile is quite flat. Note also that there is noise in  $I_b$ . However, we did not find any improvements in the fitting process by smoothing the curve.

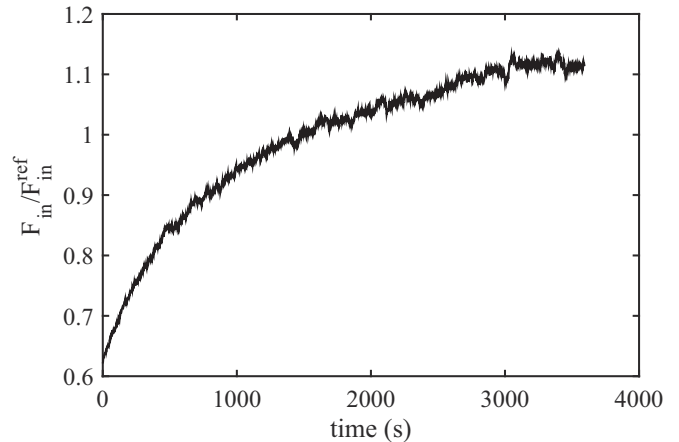


FIG. 12. Recovery curve based only on the bleached region, from the same data of Fig. 5.

Unlike common practice, we do not normalize the recovery curve between 0 and 1, because our bleaching is not complete and in this way we improve the sensitivity of the fit. The model has two fitting parameters,  $G$  and  $\tau$ , but the value of  $G$  has a large influence on the initial value of  $F^{\text{model}}$ , as shown in Fig. 11(a), while the value of  $\tau$  influences the overall shape of the curve. Thus, the use of the raw curve  $F(t)$  facilitates the fitting of  $G$ , letting, in practice,  $\tau$  as the only parameter for the shape of the recovery curve. Instead, normalized curves change very little with changes in the value of  $G$ , as shown in Fig. 11(b), and therefore the sensitivity of the fit is poorer.

Finally, a comment regarding the use of the bleached and outer regions. Since we use a fluorescence microscope, the illumination can fluctuate slightly in time, leading to noise in the fluorescence signals. This is illustrated in Fig. 12, which shows  $F_{\text{in}}/F_{\text{in}}^{\text{ref}}$  for the same data of Fig. 5. Normalization with the fluorescence recorded outside the bleached region cancels out this noise, leading to a much smoother recovery curve  $F(t)$  as shown in Fig. 5(b).

- 
- [1] N. B. Cole, C. L. Smith, N. Sciaky, M. Terasaki, M. Edidin, and J. Lippincott-Schwartz, Diffusional mobility of Golgi proteins in membranes of living cells, *Science* **273**, 797801 (1996).
- [2] M. J. Dayel, E. F. Y. Hom, and A. S. Verkman, Diffusion of green fluorescent protein in the aqueous-phase lumen of endoplasmic reticulum, *Biophys. J.* **76**, 2843 (1999).
- [3] D. A. Rusakov and D. M. Kullmann, Extrasynaptic glutamate diffusion in the hippocampus: Ultrastructural constrains, uptake, and receptor activation, *J. Neurosci.* **18**, 3158 (1998).
- [4] C. Nicholson, Diffusion and related transport mechanism in brain tissue, *Rep. Prog. Phys.* **64**, 815 (2001).
- [5] A. W. El-Kareh, S. L. Braunstein, and T. W. Secomb, Effect of cell arrangement and interstitial volume fraction on the diffusivity of monoclonal antibodies in tissue, *Biophys. J.* **64**, 1638 (1993).
- [6] H. McLennan, The diffusion of potassium, inulin, and thiocyanate in the extracellular spaces of mammalian muscle, *Biochim. Biophys. Acta* **21**, 472 (1956).
- [7] R. E. Safford and J. B. Bassingthwaite, Calcium diffusion in transient and steady states in muscle, *Biophys. J.* **20**, 113 (1977).
- [8] J. M. P. Q. Delgado, A simple experimental technique to measure tortuosity in packed beds, *Can. J. Chem. Eng.* **84**, 651 (2008).
- [9] I. F. Sbalzarini, A. Mezzacasa, A. Helenius, and P. Koumoutsakos, Effects of organelle shape on fluorescence recovery after photobleaching, *Biophys. J.* **89**, 1482 (2005).
- [10] M. J. Saxton, Lateral diffusion in a mixture of mobile and immobile particles. A Monte Carlo study, *Biophys. J.* **58**, 1303 (1990).
- [11] M. Dlugosz and J. Trylska, Diffusion in crowded biological environments: Applications of Brownian dynamics, *BMC Biophys.* **4**, 3 (2011).
- [12] M. J. Saxton, Lateral diffusion in an archipelago. Dependence on tracer size, *Biophys. J.* **64**, 1053 (1993).

- [13] L. L. Latour, K. Svodoba, P. P. Mitra, and C. H. Sotak, Time-dependent diffusion of water in a biological model system, *Proc. Natl. Acad. Sci. USA* **91**, 1229 (1994).
- [14] P.-Y. Lanfrey, Z. V. Kuzeljevic, and M. P. Dudukovic, Tortuosity model for fixed beds randomly packed with identical particles, *Chem. Eng. Sci.* **65**, 1891 (2010).
- [15] R. T. Mathias, Effect of tortuous extracellular pathways on resistance measurements, *Biophys. J.* **42**, 055 (1983).
- [16] B. P. Ölveczky and A. S. Verkman, Monte Carlo analysis of obstructed diffusion in three dimensions: Application to molecular diffusion in organelles, *Biophys. J.* **74**, 2722 (1998).
- [17] L. Tao and C. Nicholson, Maximum geometrical hindrance to diffusion in brain extracellular space surrounding uniformly spaced convex cells, *J. Theor. Biol.* **229**, 59 (2004).
- [18] N. A. Vrettos, H. Imakoma, and M. Okazaki, An effective medium treatment of the transport properties of a Voronoi tessellated network, *J. Appl. Phys.* **66**, 2873 (1989).
- [19] N. A. Vrettos, H. Imakoma, and M. Okazaki, Effective medium approximation of 3-D Voronoi networks, *J. Appl. Phys.* **67**, 3249 (1990).
- [20] M. Sahimi and T. Tsotsis, Transient diffusion and conduction in heterogeneous media: Beyond the classical effective-medium approximation, *Ind. Eng. Chem. Res.* **36**, 3043 (1997).
- [21] J. Deng, D. Morgan, and I. Szlufarska, Kinetic Monte Carlo simulation of the effective diffusivity in grain boundary networks, *Comput. Mater. Sci.* **93**, 36 (2014).
- [22] R. Peters, J. Peters, K. H. Tews, and W. Bähr, A microfluorimetric study of translational diffusion in erythrocyte membranes, *Biochim. Biophys. Acta* **367**, 282 (1974).
- [23] K. Jacobson, E. Wu, and G. Poste, Measurement of the translational mobility of Concanavalin A in glycerol-saline solutions and on the cell surface by fluorescence recovery after photobleaching, *Biochim. Biophys. Acta* **433**, 215 (1976).
- [24] J. Lippincott-Schwartz, E. Snapp, and A. Kenworthy, Studying protein dynamics in living cells, *Nature Rev. Mol. Cell Biol.* **2**, 444 (2001).
- [25] E. A. J. Reits and J. J. Neefjes, From fixed to FRAP: Measuring protein mobility and activity in living cells, *Nature Cell Biol.* **3**, E145 (2001).
- [26] M. Wu, F. Xiao, R. M. Johnson-Paben, S. T. Retterer, X. Yin, and K. B. Neeves, Single- and two-phase flow in microfluidic porous media analogs based on Voronoi tessellation, *Lab Chip* **12**, 253 (2012).
- [27] H. X. Zhu, S. M. Thorpe, and A. H. Windle, The geometrical properties of irregular two-dimensional Voronoi tessellations, *Phil. Mag. A* **81**, 2765 (2001).
- [28] J. C. McDonald, D. C. Duffy, J. R. Anderson, D. T. Chiu, H. Wu, O. J. A. Schueller, and G. M. Whitesides, Fabrication of microfluidic systems in poly(dimethylsiloxane), *Electrophoresis* **21**, 27 (2000).
- [29] C. T. Culbertson, S. C. Jacobson, and J. M. Ramsey, Diffusion coefficient measurements in microfluidic devices, *Talanta* **56**, 365 (2002).
- [30] A. Axelrod, D. E. Koppel, J. Schlessinger, E. Elson, and W. W. Webb, Mobility measurement by analysis of fluorescence photobleaching recovery kinetics, *Biophys. J.* **16**, 1055 (1976).
- [31] D. M. Soumpasis, Theoretical analysis of fluorescence photobleaching recovery experiments, *Biophys. J.* **41**, 95 (1983).
- [32] T. Cui-Wang, C. Hanus, T. Cui, T. Helton, J. Bourne, D. Watson, K. M. Harris, and M. D. Ehlers, Local zones of endoplasmic reticulum complexity confine cargo in neuronal dendrites, *Cell* **148**, 309 (2012).
- [33] M. J. Saxton, Lateral diffusion in an archipelago. Distance dependence of the diffusion coefficient, *Biophys. J.* **56**, 615 (1989).
- [34] D. Blumenthal, L. Goldstien, M. Edidin, and L. A. Gheber, Universal approach to FRAP analysis of arbitrary bleaching patterns, *Sci. Rep.* **5**, 11655 (2015).